

Midinfrared semiconductor optical metamaterials

Anthony J. Hoffman,^{1,a)} Aishwarya Sridhar,¹ Phillip X. Braun,¹ Leonid Alekseyev,^{1,2} Scott S. Howard,¹ Kale J. Franz,¹ Liwei Cheng,³ Fow-Sen Choa,³ Deborah L. Sivco,⁴ Viktor A. Podolskiy,⁵ Evgenii E. Narimanov,^{1,2} and Claire Gmachl^{1,b)}

¹*Department of Electrical Engineering, Princeton University, Princeton, New Jersey 08544, USA*

²*School of Electrical and Computer Engineering, Purdue University, West Lafayette, Indiana 47907, USA*

³*Department of Computer Science and Electrical Engineering, University of Maryland Baltimore County, Maryland 21250, USA*

⁴*Alcatel-Lucent, Murray Hill, New Jersey 07974, USA*

⁵*Department of Physics, Oregon State University, Corvallis, Oregon 97331, USA*

(Received 16 October 2008; accepted 2 April 2009; published online 18 June 2009)

We report on a novel class of semiconductor metamaterials that employ a strongly anisotropic dielectric function to achieve negative refraction in the midinfrared region of the spectrum, $\sim 8.5\text{--}13\ \mu\text{m}$. We present two types of metamaterials, layered highly doped/undoped heterostructures and quantum well superlattices that are highly anisotropic. Contrary to other optical metamaterials these heterostructure systems are optically thick (up to $20\ \mu\text{m}$ thick), planar, and require no additional fabrication steps beyond the initial growth. Using transmission and reflection measurements and modeling of the highly doped heterostructures, we demonstrate that these materials exhibit negative refraction. For the highly doped quantum well superlattices, we demonstrate anomalous reflection due to the strong anisotropy of the material but a determination of the sign of refraction is still difficult. This new class of semiconductor metamaterials has great potential for waveguiding and imaging applications in the long-wave infrared.

© 2009 American Institute of Physics. [DOI: [10.1063/1.3124087](https://doi.org/10.1063/1.3124087)]

I. INTRODUCTION

An optical metamaterial is a composite in which sub-wavelength features, along with the constituent materials, control the macroscopic electromagnetic properties of the material. Recently, metamaterials have attracted much interest because of their unusual interaction with electromagnetic waves. Newly invented metamaterials open new opportunities to the optical engineer to design novel properties for optical materials demonstrating unusual optical phenomena and unique applications. One example of these materials are the so-called “negative index materials” (NIMs).^{1,2} When light crosses the interface between a NIM and a conventional material, it refracts to the same side of the surface normal as it was initially incident. This immediately opens up the possibility of planar lens design.^{1,3} Under some additional constraints, such a lens may have a resolution limit that is no longer determined by the wavelength of the light.^{3,4}

Negative index materials, as first proposed¹ and recently demonstrated in the laboratory,^{4,5} required the permittivity, ϵ , and permeability, μ , to be simultaneously less than zero, and achieved that by an intricate pattern of metallic nanoresonators.^{6–9} While originally demonstrated in the microwave region of the spectrum, recent designs exhibit negative refraction in the near-infrared and optical frequencies.^{10–13} These materials still rely upon overlapping resonances in ϵ and μ , and require intricate nanofabrication. One strategy to greatly ease the design and fabrication and reduce loss is to create a material with only a single reso-

nance, e.g., in ϵ . For these materials, however, a second optical characteristic, such as anisotropy or chirality, is employed to produce negative refraction, thus distinguishing it from naturally occurring resonant materials.^{14,15}

We have recently demonstrated an all-semiconductor approach to achieving negative refraction in the long-wave infrared using a superlattice with an anisotropic dielectric function and an electric resonance.¹⁶ Here we extend this work to significantly thicker ($20\ \mu\text{m}$) structures and present a second approach based on intersubband transitions in quantum wells. Both metamaterials are semiconductor-based and employ a single epitaxial growth process, thus eliminating the need for additional nanofabrication. The materials are inherently three-dimensional and planar, and the operational wavelength range is determined by the free carrier density and layer thicknesses, both easily controlled parameters in the material growth. Metamaterials composed of highly doped heterostructures exhibit negative refraction for a large bandwidth in the far infrared. Metamaterials composed of degenerately doped quantum wells display anomalous reflection in the spectral regime where negative refraction is anticipated; however, determination of the sign of refraction is difficult and unknown.

In anisotropic materials, the electric field vector, \mathbf{E} , and the electric displacement vector, \mathbf{D} , are not usually parallel. An immediate consequence of this is that the Poynting vector, \mathbf{S} , which points in the direction of energy flow and wave vector, \mathbf{k} , directed along the wave front normal, need not be parallel. Since the boundary conditions at the interface of two materials require only that the tangential component of \mathbf{k} is conserved, it is possible for the refracted beam to exhibit

^{a)}Electronic mail: ajhoffma@princeton.edu.

^{b)}Electronic mail: cgmachl@princeton.edu.

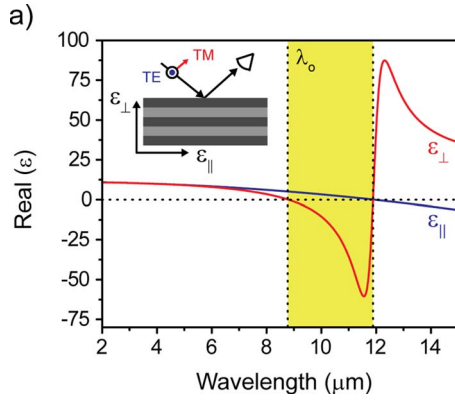


FIG. 1. (Color online) Calculated permittivity tensor, $\epsilon_{||}$ and ϵ_{\perp} , using the effective medium approximation for an n^+ -InGaAs/ i -AlInAs sample with $n_d = 7.5 \times 10^{18} \text{ cm}^{-3}$. The shaded yellow region shows the spectral region where the anisotropy results in negative refraction for all angles of incidence. The inset shows the orientation of the electric field and the components of the permittivity; from Ref. 16.

normal (positive) refraction with respect to \mathbf{k} but negative refraction with respect to \mathbf{S} .^{17,18} The directions of the vectors \mathbf{k} and \mathbf{S} in the refracted beam will be related to the angle of incidence, θ_i , through a Snell's law-like relation. In the limit of low material absorption, the effective phase and group indices of an anisotropic system are given by

$$n_k = \sqrt{\epsilon_{||} + \left(1 - \frac{\epsilon_{||}}{\epsilon_{\perp}}\right) \sin^2 \theta_i};$$

$$n_S = \frac{\epsilon_{\perp}}{\epsilon_{||}} \sqrt{\epsilon_{||} + \left(\frac{\epsilon_{||}^2}{\epsilon_{\perp}^2} - \frac{\epsilon_{||}}{\epsilon_{\perp}}\right) \sin^2 \theta_i},$$

where $\epsilon_{||}$ and ϵ_{\perp} are the components of the permittivity relative to the surface of the material [see Fig. 1(a) inset for definition].

A uniaxial anisotropic material with $\epsilon_{||} > 0$ and $\epsilon_{\perp} < 0$ will exhibit negative refraction with respect to \mathbf{S} for the transverse magnetic (TM) polarization for *all* incidence angles. Such a material is exceptionally different from other anisotropic materials that may exhibit negative refraction for only a small range of incidence angles.¹⁹ Furthermore, this behavior is different from an isotropic NIM, $\epsilon, \mu < 0$, where both \mathbf{S} and \mathbf{k} refract negatively. Since the transverse electric (TE) polarization does not experience anisotropy, both \mathbf{k} and \mathbf{S} refract normally.¹⁵

II. HIGHLY DOPED HETEROSTRUCTURES

The required anisotropy, $\epsilon_{\perp} < 0 < \epsilon_{||}$, has been realized in n^+ - i - n^+ semiconductor heterostructures with appropriately thick layers that have alternating positive and negative dielectric constants. The thickness of the layers is chosen to be sufficiently large so that quantization of the energy levels in the system is irrelevant, but also thin enough, much smaller than the wavelength, so that the effective medium approximation is applicable. Such materials are straightforward to design as the region of negative refraction depends upon the well-understood isotropic permittivities of the alternating layers.

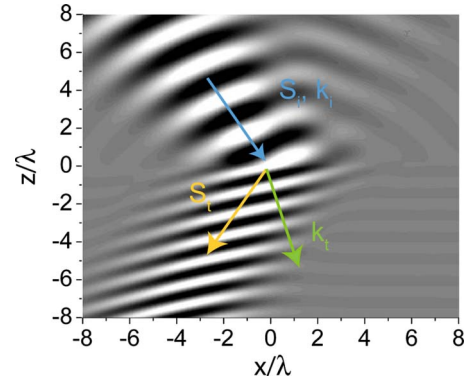


FIG. 2. (Color online) Numerical calculations of refraction across an air-metamaterial interface for a monochromatic, TM polarized Gaussian beam; from Ref. 16.

A. Numerical calculations of microscopic optical properties

The effective permittivity tensor for heterostructures composed of i -AlInAs and n^+ -InGaAs is uniaxial, and the two components, $\epsilon_{||}$ and ϵ_{\perp} , are related to the isotropic permittivities ϵ_{InGaAs} and ϵ_{AlInAs} as follows:

$$\epsilon_{||} = \frac{\epsilon_{\text{InGaAs}} + \epsilon_{\text{AlInAs}}}{2}, \quad \epsilon_{\perp} = \frac{2\epsilon_{\text{InGaAs}}\epsilon_{\text{AlInAs}}}{\epsilon_{\text{InGaAs}} + \epsilon_{\text{AlInAs}}}$$

The i -AlInAs and n^+ -InGaAs isotropic permittivities are approximated by using a constant permittivity for the AlInAs layers and the Drude model for the doped InGaAs layers. Thus, $\epsilon_{\text{AlInAs}} = \epsilon_{\infty-\text{AlInAs}}$ and $\epsilon_{\text{InGaAs}}(\omega) = \epsilon_{\infty-\text{InGaAs}}[1 - \omega_p^2/(\omega^2 - i\omega/\gamma)]$, where $\epsilon_{\infty-\text{AlInAs}} = 10.23$ and $\epsilon_{\infty-\text{InGaAs}} = 12.15$ are the high frequency permittivities of the respective materials, ω_p is the plasma frequency, and $\gamma = 0.1 \times 10^{-12} \text{ s}^{-1}$ is the damping parameter; $\epsilon_{\text{InGaAs}} = 0$ at λ_o , the wavelength corresponding to ω_p , and the value of λ_o decreases with increasing doping density, n_d .

Far from the plasma frequency of the InGaAs layers, $\epsilon_{||}$ approximately equals ϵ_{\perp} , and the sample behaves as an isotropic material with an effective permittivity approximately equal to $(\epsilon_{\text{InGaAs}} + \epsilon_{\text{AlInAs}})/2$. As the wavelength increases and approaches the plasma frequency of the isotropic InGaAs layers, ϵ_{\perp} decreases, eventually becoming negative for $\lambda > \lambda_o$. Figure 1 shows a plot of $\epsilon_{||}$ and ϵ_{\perp} as a function of wavelength. The solid lines correspond to the real parts of the permittivity and the inset shows the definition of the TM and TE polarizations as well as the direction of the components of the effective permittivity tensor. The spectral interval where the metamaterial exhibits negative refraction is indicated by the shaded yellow region. Figure 2 shows full numerical calculations for the refraction of a monochromatic Gaussian beam across the air/metamaterial interface in the negative refraction regime.

B. Numerical calculations of macroscopic optical properties

The onset of negative refraction strongly influences macroscopic properties such as reflection and transmission. Using the values for $\epsilon_{||}$ and ϵ_{\perp} with $n_d = 7.5 \times 10^{18} \text{ cm}^{-3}$ and an anisotropic transfer matrix method, we calculate the reflec-

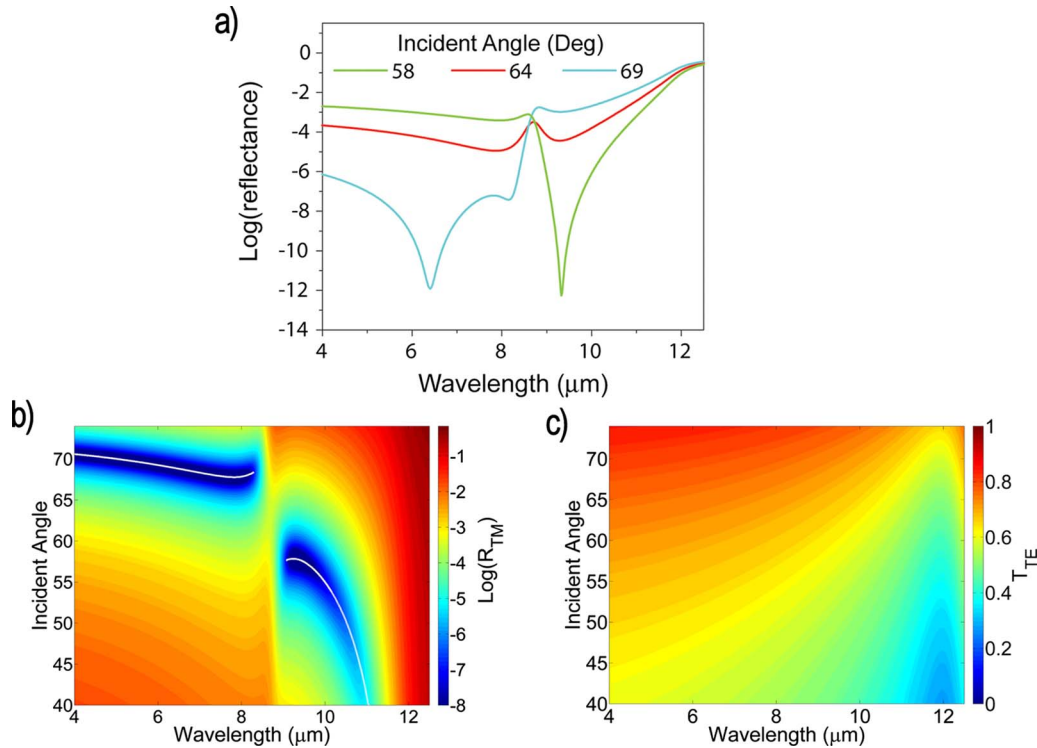


FIG. 3. (Color online) (a) Select traces of the TM reflectance, R_{TM} , vs wavelength for a simulated half-infinite metamaterial with $n_d = 7.5 \times 10^{18} \text{ cm}^{-3}$ and $\lambda_o = 8.8 \text{ } \mu\text{m}$ for light incident from air. (b) Logarithmic color plot of R_{TM} vs wavelength and incidence angle assembled from many traces such as those in (a). The solid white curve marks the angle corresponding to the Brewster angle for each wavelength. (c) Calculated TE reflectance vs wavelength and incident angle for the same metamaterial as above.

tance as a function of wavelength and incident angle for both polarizations for a half-infinite slab of material. Figure 3(a) displays several reflectance-versus-wavelength curves of the calculated data for the TM polarization on a logarithmic scale. The strong minima in the 58° and 69° curves result from the Brewster angle conditions being met at these wavelengths and incident angles. The different spectral locations of the minima are due to the frequency dependent permittivity of the metamaterial. The lack of a similar, well-defined minimum in the 64° curve shows a discontinuity of the Brewster angle. Figure 3(b) depicts the TM reflectance, R_{TM} , of the metamaterial as a function of wavelength and incident angle in a log-scale color plot. The Brewster angle, which is marked by the solid white line, exhibits a discontinuity at $\lambda_o = 8.8 \text{ } \mu\text{m}$. This wavelength corresponds to $\epsilon_{\perp} \approx 0$ and marks the beginning of the interval where negative refraction will occur.

The discontinuity of the Brewster angle is a characteristic property of TM-polarized light in a strongly anisotropic metamaterial. Isotropic, highly doped materials, with an electric resonance at the same wavelength, do not exhibit such a feature. Rather, for these materials, the Brewster angle changes continuously with wavelength. The reflectance of the TE polarization, R_{TE} , does not exhibit a Brewster angle or any discontinuities, and hence serves as a suitable spectral reference. A plot of the calculated R_{TE} versus wavelength and incident angle is shown in Fig. 3(c).

Calculations of the transmission through a slab of anisotropic metamaterial $8.08 \text{ } \mu\text{m}$ thick on top of an InP substrate for the same dielectric tensor were also performed.

Figure 4(a) displays calculated TM transmittance spectra, T_{TM} , versus wavelength for three incidence angles, 10°, 37°, and 74°, and Fig. 4(b) is a color plot of transmittance versus wavelength and incident angle assembled from many such curves. In both figures, the fringes are due to interference effects across the epitaxial layer, and the overall decrease in transmission with increasing wavelength is due to increasing free carrier absorption. The strong dip in the transmission around the critical wavelength $\lambda_o = 8.8 \text{ } \mu\text{m}$ is due to the increasing imaginary component of the wave vector, which is related to loss, as the real part of ϵ_{\perp} approaches 0. Beyond the resonance, the increase in transmission is due to a decrease in the loss as ϵ_{\perp} becomes increasingly negative. Such behavior is indicative of the anisotropy of our metamaterial.

C. Sample design and characterization

To achieve negative refraction at midinfrared wavelengths, we designed and fabricated six samples composed of interleaved 80 nm layers of $\text{In}_{0.53}\text{Ga}_{0.47}\text{As}$ and $\text{Al}_{0.48}\text{In}_{0.52}\text{As}$. Five of the samples, A–E, were grown by molecular beam epitaxy (MBE) on lattice-matched InP substrates. Samples A–D, reported earlier in Ref. 16, are $8.08 \text{ } \mu\text{m}$ thick and sample E is $20 \text{ } \mu\text{m}$ thick. The sixth sample, F, was grown by metal-organic chemical vapor deposition (MOCVD) on InP and is $8.08 \text{ } \mu\text{m}$ thick. The InGaAs layers were uniformly doped, at different densities for each sample, to provide a plasma resonance of free carriers. For each sample, the free carrier density of the InGaAs layers, n_d , was extracted from transmission measurements by identifying the spectral loca-

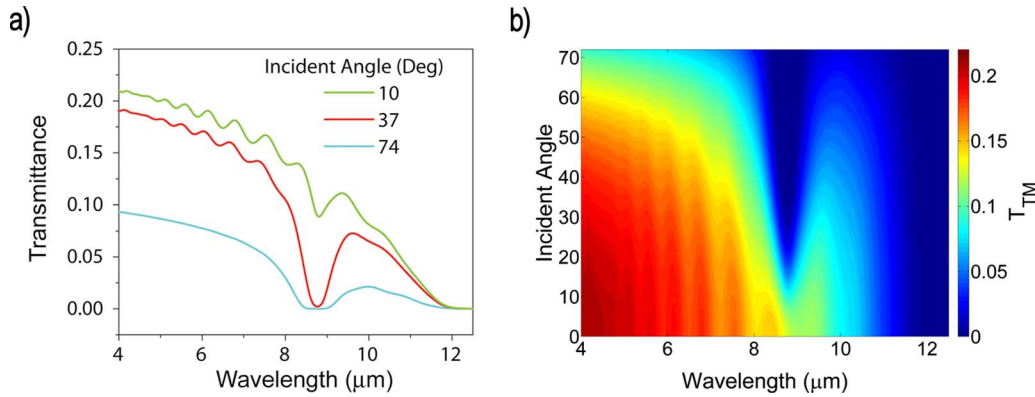


FIG. 4. (Color online) (a) Select traces of the TM transmittance, T_{TM} , for a simulated metamaterial with $n_d = 7.5 \times 10^{18} \text{ cm}^{-3}$ and a thickness of 8.08 μm on top of an InP substrate for light incident from air. (b) Color plot of T_{TM} vs wavelength and incidence angle assembled from many traces as those shown in (a).

tion of the minimum in the previously described dip [see Fig. 4(a)]. The so-extracted densities for our samples, A–F, are 3.4×10^{18} , 5.7×10^{18} , 7.1×10^{18} , 7.5×10^{18} , 8.3×10^{18} , and $3.3 \times 10^{18} \text{ cm}^{-3}$ resulting in critical wavelengths of 13.1, 10.1, 9.1, 8.8, 8.4, and 13.3 μm , respectively. Figure 5 summarizes n_d , λ_o , and the negative refraction bandwidth for our metamaterial samples. We also prepared a control sample, which is composed of a single $\sim 4.7 \text{ μm}$ thick InGaAs layer doped $5.8 \times 10^{18} \text{ cm}^{-3}$. This sample and a low-doped InP substrate serve as isotropic controls.

We conducted reflection and transmission measurements as a function of polarization, incident angle, and wavelength. A Fourier transform infrared (FTIR) spectrometer, ZnSe or Ge lenses, and a liquid nitrogen cooled mercury-cadmium-telluride detector were used for all measurements. The light from the FTIR source was focused onto the sample and the reflected or transmitted light was collected on the detector.

For the reflection measurements, the specular reflection for light incident on the epitaxial layer was measured from 40° to 74° in 2° increments for each metamaterial sample and the high-doped control. The data are analyzed as the ratio of TM to TE with the purpose of minimizing environmental fluctuations. Figure 6(a) plots the experimental reflection measurements for sample E, the 20 μm thick

sample with a doping density of $8.3 \times 10^{18} \text{ cm}^{-3}$ and $\lambda_o = 8.4 \text{ μm}$, in a log-scale color plot versus incident angle and wavelength. The discontinuity around 8.4 μm is due to a discontinuity in the TM-polarized response and occurs in the expected spectral range where $\epsilon_\perp \approx 0$. The remaining metamaterial samples, except for sample F grown by MOCVD, also display discontinuities in R_{TM} at their respective critical wavelengths and agree well with theoretical calculations. Results for a similar analysis of the isotropic, highly doped control sample are shown in Fig. 6(b); there is no discontinuity in the Brewster angle with wavelength. Sample F does display a weak discontinuity in R_{TM} as a function of wavelength as shown in Fig. 6(c); however, it lacks a discontinuity in R_{TM} as a function of incident angle (a characteristic of all the remaining samples). Secondary ion mass spectroscopy measurements indicate that Si dopant atoms are present in the top AlInAs layers and we suspect that the doping level is not uniform throughout the sample. The optical characteristics of this sample are still under investigation.

Using the reflection measurements, we determined the bandwidth of the spectral region that exhibits negative refraction. The short-wavelength limit of the region is marked by the discontinuity of the Brewster angle and the long-wavelength limit is marked by a large increase in the reflectivity. This increase, which approaches unity for long wavelengths, is due to both the real parts of ϵ_\parallel and ϵ_\perp approaching 0 (see Fig. 1(a), $\lambda = 11.8 \text{ μm}$) and their growing imaginary parts. We use 50% TE reflectivity for an incident angle of 40° to mark the end of the region. The bandwidth about the central wavelength of the region for all the samples is between 27% and 29% (for the lower doped samples, A and F, the long-wavelength limit was calculated using the theoretical model because it was located beyond the detector cutoff).

Transmission measurements were performed on the metamaterial samples, and spectra as a function of polarization, incident angle, and wavelength were collected for incident angles from 0° to 74° in 2° increments. For all transmission measurements, the light was incident upon the epitaxial side and the substrate side was mirror polished to minimize surface scattering. The background-corrected data were analyzed as the ratio of TM over TE. Experimental results for sample E are shown in Fig. 7(a). The main feature

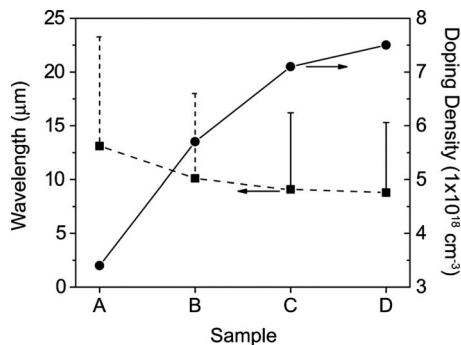


FIG. 5. Summary of the samples characterized in the study. The filled symbols are for samples grown by MBE and the open symbols are for the sample grown by MOCVD. The squares show the critical wavelength, λ_o , for the different samples and the vertical bars indicate the extent of the spectral region with negative refraction; the dashed bars indicate that the long wavelength limit was extrapolated using a theoretical model because the region was beyond the detector cutoff. The circles represent the extracted doping density from transmission measurements.

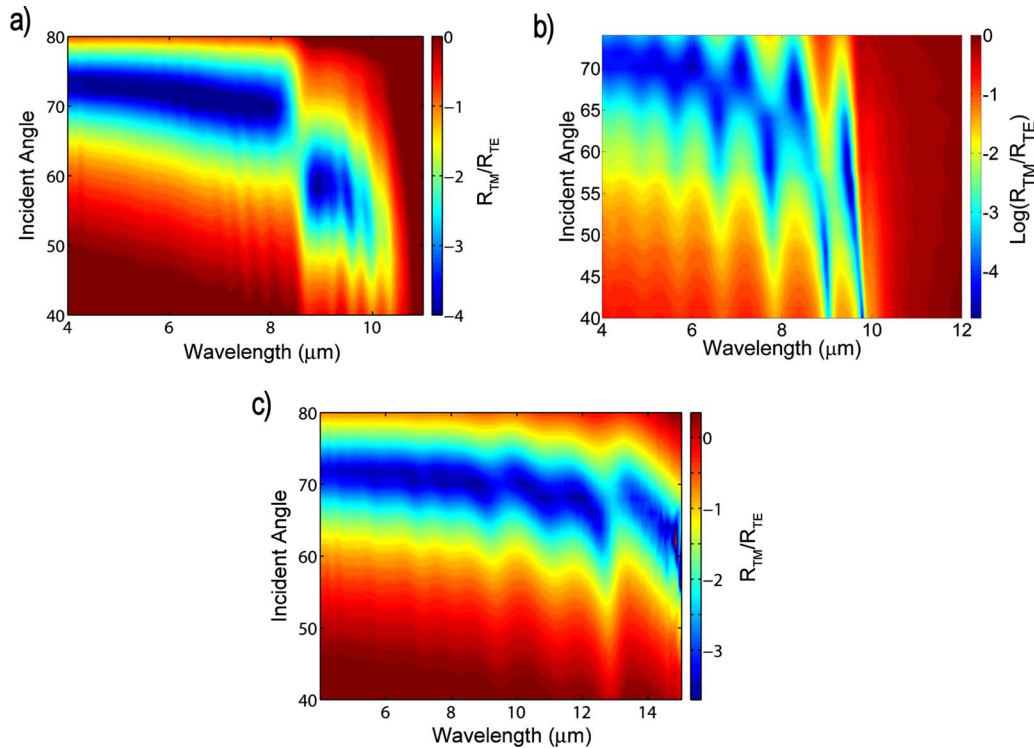


FIG. 6. (Color online) (a) Measured TM/TE reflectance for sample E with an epitaxial thickness of 20 μm and $n_d = 8.3 \times 10^{18} \text{ cm}^{-3}$. (b) Measured TM/TE reflectance for the high-doped, $n_d = 5.8 \times 10^{18} \text{ cm}^{-3}$, isotropic control. (c) Measured TM/TE reflectance for sample F grown by MOCVD with $n_d \sim 3.3 \times 10^{18} \text{ cm}^{-3}$.

is the minimum in the ratio around the transition wavelength $\lambda_o = 8.4 \mu\text{m}$, resulting from the dip in the TM transmission. The presence of this feature and its spectral location agrees very well with the reflection measurements and our theoretical model of the metamaterial.

To characterize the optical loss of the metamaterials, we used both the transmission and reflection measurements to estimate the absorption coefficient for the TM polarization, α_{TM} , at the peak-transmission wavelength in the negative refraction regime, i.e., $\sim 9.9 \mu\text{m}$ for sample D. The measured losses were compared with theoretical values obtained using an anisotropic transfer matrix. For both experiment and theory $\alpha_{\text{TM}} \approx -\ln[T_{\text{TM}}/(1-R_{\text{TM}})]/L$, where T_{TM} and R_{TM} are the TM transmittance and reflectance, respectively, and L is the thickness of the metamaterial. For sample D, the measured loss for an incident angle of 40° is 1800 cm^{-1} and increases approximately linearly with increasing incident

angle to 2100 cm^{-1} at 60° . The measured loss is approximately 15% greater than the theoretical prediction. Regardless, even for the 20 μm thick metamaterial, transmission through the sample was measured with a good signal to noise ratio.

III. DEGENERATELY DOPED QUANTUM WELL SUPERLATTICE

A quantum well superlattice will exhibit intersubband absorption for the TM polarization at wavelengths corresponding to allowed transitions between energy levels. The strength of the absorption is affected by the oscillator strength, population difference between the subbands, and the dephasing time.²⁰ The population difference can be directly controlled by the doping density and the dephasing time is made large by high quality growth. Since an absorption resonance is necessarily accompanied by a change in the permittivity, it may be possible to obtain the requisite anisotropy, $\epsilon_{\parallel} < 0 < \epsilon_{\perp}$, for a sufficiently strong and narrow absorption resonance.

A. Sample design

To examine the possibility of negative refraction in these materials, we designed, grew by MBE, and characterized three InGaAs/AlInAs quantum well samples consisting of 85 Å wells and barriers with the wells doped $> 1 \times 10^{19} \text{ cm}^{-3}$ and a control sample with the same well and barrier thicknesses but doped only $2 \times 10^{17} \text{ cm}^{-3}$. All of the samples were grown on InP and the epitaxial growth was approximately 5 μm thick. The energy difference between

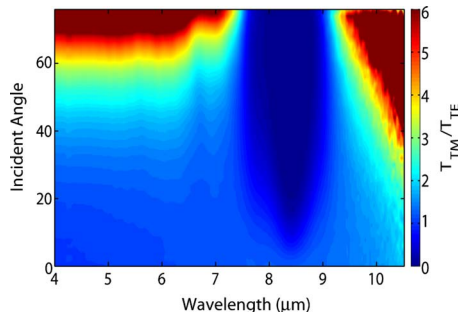


FIG. 7. (Color online) Measured TM/TE transmittance vs wavelength and incidence angle for sample E with an epitaxial thickness of 20 μm and $n_d = 8.3 \times 10^{18} \text{ cm}^{-3}$.

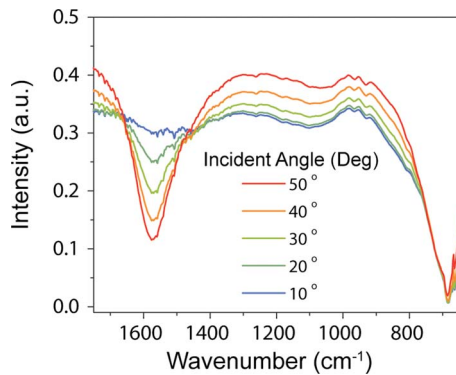


FIG. 8. (Color online) Measured TM transmission spectra of a degenerately doped quantum well superlattice for several incident angles.

the ground state and the first excited state, E_{21} , and the first excited state and the second excited state, E_{32} , were calculated as 158 and 192 meV neglecting electron-electron interactions. These transition energies correspond to wave numbers of 1274 and 1548 cm^{-1} , respectively.

B. Sample characterization

The energy levels of the quantum well superlattices were determined using angle-dependent transmission spectra. Figure 8 shows transmission measurements for the TM polarization at several angles of incidence. A dip in the transmission around 1570 cm^{-1} or 195 meV increases in strength with increasing incident angle. This feature corresponds to the E_{32} intersubband transition. At normal incidence, the electric field of the incident light cannot interact with the dipole of the quantum well and the intersubband absorption is minimal; however, as the incidence angle increases, the interaction between the quantum well and the light becomes stronger and photons of appropriate energies are absorbed. This transition energy is consistent with our quantum mechanical calculations for E_{32} of 192 meV. A similar dip corresponding to the E_{21} transition is not observed. This lack of a feature is attributed to Fermi blocking due to the high free carrier density and the room temperature thermal distribution of the free electrons. The decrease in the transmission spectra for wave numbers greater than 900 cm^{-1} for all incident angles is attributed to absorption from a plasmlike resonance in the quantum wells due to the high free carrier density.

Reflectance as a function of polarization, wave number, and incident angle was also measured for all four samples. The data were analyzed as the ratio of R_{TM} over R_{TE} to minimize background fluctuations. Measurements for a highly doped sample and the control sample are shown in Figs. 9(a) and 9(b), respectively. For both samples, fringes due to interference effects are observed. For the highly doped sample, a deep blue region with a minimum (darkest blue) around 1600 cm^{-1} is observed. This is due primarily to a dip in the TM reflectance, which is attributed to the large intersubband absorption corresponding to the E_{32} transition. Such a feature is not observed in the low-doped control because of the smaller population difference between the subbands and thus the weaker intersubband absorption. Finally, for the high-doped material, a region of anomalous reflection in the

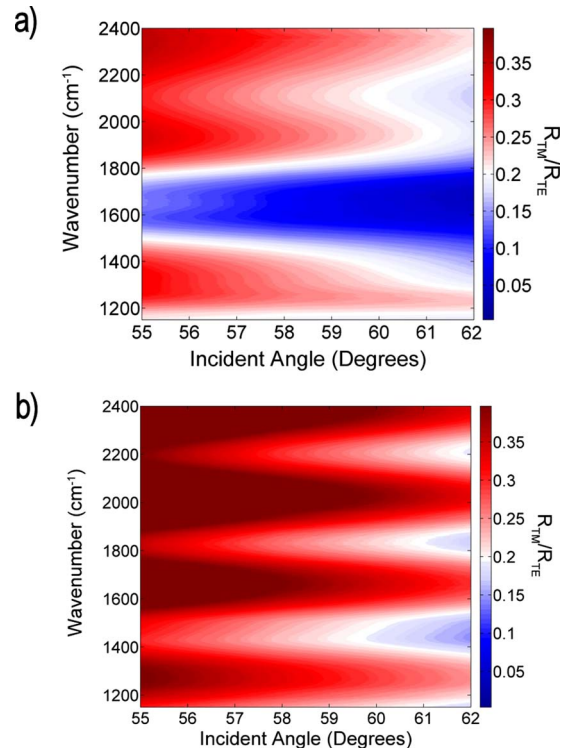


FIG. 9. (Color online) (a) Measured TM/TE reflectance vs incident angle and wavelength for a degenerately doped quantum well superlattice. (b) Measured TM/TE reflectance vs incident angle and wavelength for a quantum well superlattice doped $2 \times 10^{17} \text{ cm}^{-3}$.

vicinity of the E_{21} transition, 1280 cm^{-1} , is observed as an asymmetry in an interference fringe. The asymmetry is due to an increase in the TM reflectance, which in turn is due to a rapid change in the dielectric function. The spectral location of the enhanced reflection agrees well with the calculated E_{21} transition, but a determination of the actual dielectric function is difficult.

Low reflection resonances not related to negative refraction are also observed far from the intersubband absorption resonances. Figures 10(a) and 10(b) show the resonances as a function of angle for the TE and TM polarizations, respectively; the strength and spectral location of the resonances depend weakly upon the incident angle. Control over the TE and TM resonances by thinning of the epitaxial layer to $\sim 2.7 \mu\text{m}$ and application of a SiN_x dielectric is shown in Figs. 10(c) and 10(d), respectively. In the case of the TM polarization, the resonance is eliminated by application of a 1600 Å SiN_x film. For the TE polarization and the same film thickness, the resonance redshifts and increases in strength significantly.

IV. CONCLUSION

We have studied a new class of anisotropic semiconductor metamaterials that have the potential for negative refraction in the midinfrared. The materials are three-dimensional, planar, and require no additional nanofabrication beyond the initial growth. Metamaterials composed of highly doped heterostructures were shown to exhibit negative refraction across a wide range of wavelengths and the region of negative refraction was controlled by adjusting growth param-

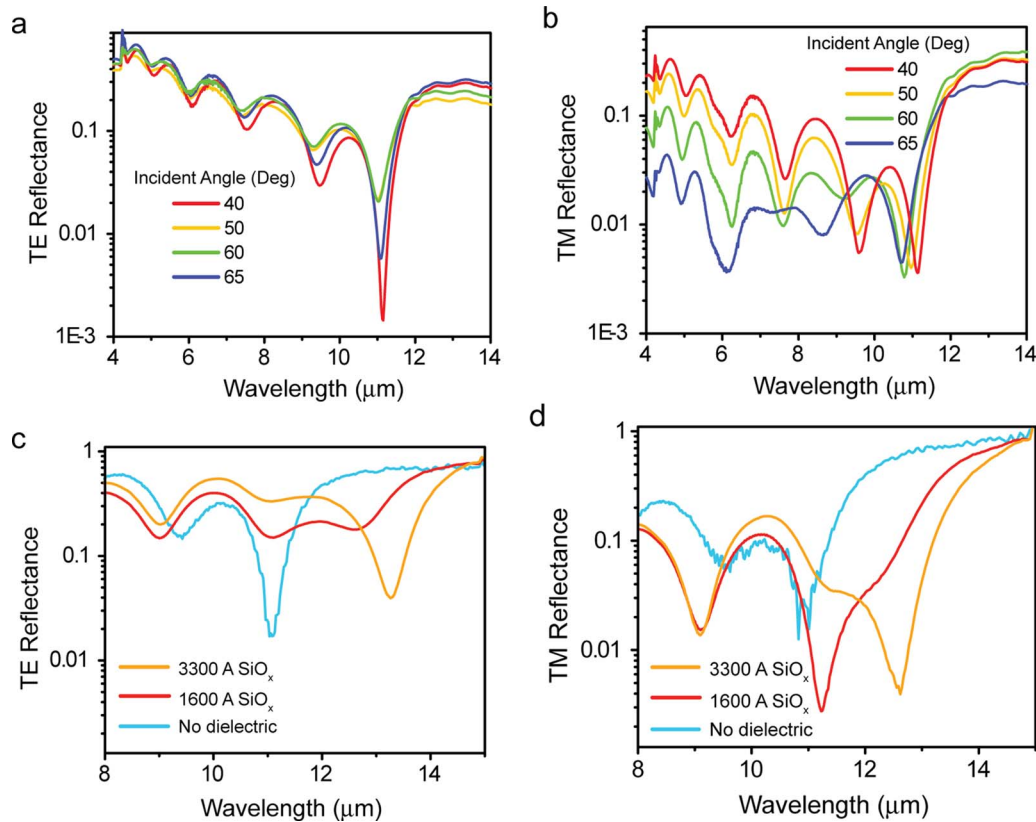


FIG. 10. (Color online) Measured (a) TE and (b) TM reflectance of degenerately doped quantum wells exhibiting low reflection resonances for several incident angles. Measured (c) TE and (d) TM reflectance after partial removal of the epitaxial layer and application of SiO_x of different thicknesses.

eters. Degenerately doped quantum well superlattices displayed anomalous reflection in the spectral region where negative refraction was expected, but a determination of dielectric function and the sign of refraction were not possible. Such metamaterials have great potential for waveguiding and imaging applications.

ACKNOWLEDGMENTS

The authors would like to thank PRISM, PCCM (Grant No. DMR-0819860), NSF (Grant Nos. EEC-0540832 and ECCS-0724763), ONR (Grant No. N00014-07-1-0457), and ARO-MURI for support of this project.

¹V. G. Veselago, *Sov. Phys. Uspekhi* **10**, 509 (1968).

²J. B. Pendry, A. J. Holden, D. J. Robbins, and W. J. Stewart, *IEEE Trans. Microwave Theory Tech.* **47**, 2075 (1999).

³J. B. Pendry, *Phys. Rev. Lett.* **85**, 3966 (2000).

⁴D. R. Smith, W. J. Padillia, D. C. Vier, S. C. Nemat-Nasser, and S. Schultz, *Phys. Rev. Lett.* **84**, 4184 (2000).

⁵R. A. Shelby, D. R. Smith, and S. Schultz, *Science* **292**, 77 (2001).

⁶H. O. Moser, B. D. F. Casse, O. Whilhelmi, and B. T. Saw, *Phys. Rev.*

Lett. **94**, 063901 (2005).

⁷M. W. Klein, C. Enkrich, M. Wegener, and S. Linden, *Science* **313**, 502 (2006).

⁸P. Gay-Balmaz and O. J. F. Martin, *J. Appl. Phys.* **92**, 2929 (2002).

⁹T. Koschny, M. Kafesaki, E. N. Economou, and S. M. Soukoulis, *Phys. Rev. Lett.* **93**, 107402 (2004).

¹⁰V. M. Shalae, W. Cai, U. K. Chettiar, H. Yuan, A. K. Sarychev, V. P. Drachev, and A. K. Kildishev, *Opt. Lett.* **30**, 3356 (2005).

¹¹S. Zhang, W. Fan, N. C. Panoiu, K. J. Malloy, R. M. Osgood, and S. R. J. Brueck, *Phys. Rev. Lett.* **95**, 137404 (2005).

¹²S. Zhang, W. Fan, K. J. Malloy, and S. R. J. Brueck, *J. Opt. Soc. Am. B* **23**, 434 (2006).

¹³V. M. Shalae, *Nat. Photonics* **1**, 41 (2007).

¹⁴J. B. Pendry, *Science* **306**, 1353 (2004).

¹⁵V. A. Podolskiy and E. E. Narimanov, *Phys. Rev. B* **71**, 201101 (2005).

¹⁶A. J. Hoffman, L. Alekseyev, S. S. Howard, K. J. Franz, D. Wasserman, V. A. Podolskiy, E. E. Narimanov, D. L. Sivco, and C. Gmachl, *Nature Mater.* **6**, 946 (2007).

¹⁷I. V. Lindell, S. A. Tretyakov, K. I. Nikoskinen, and S. Ilvonen, *Micro-wave Opt. Technol. Lett.* **31**, 129 (2001).

¹⁸V. G. Veselago and E. E. Narimanov, *Nature Mater.* **5**, 759 (2006).

¹⁹T. M. Grzegorzczak, M. Nikku, X. Chen, B. Wu, and J. A. Kong, *IEEE Trans. Microwave Theory Tech.* **53**, 1443 (2005).

²⁰G. Almog, A. Shakouri, and A. Yariv, *Appl. Phys. Lett.* **63**, 2720 (1993).